Comprehensive Prognostic Evaluation of Spacecraft Reaction Wheels Post-Fault Occurrences

Arsh Nadkarni
Ridgetop Group
3580 W Ina Rd, Tucson, Arizona 85741
Email: anadkarni@ridgetopgroup.com

Anubhav Gupta
Aerospace Engineering Sciences
University of Colorado Boulder
Email: anubhav.gupta@colorado.edu

Wyatt Pena
Ridgetop Group
3580 W Ina Rd, Tucson, Arizona 85741
Email: wpena@ridgetopgroup.com

Abstract—**This paper investigates the influence of environmental and operational variables on the longevity of spacecraft components, with a specific focus on estimating Remaining Useful Life (RUL), Prognostic Horizon (PH), and State-of-Health (SoH) for reaction wheels afflicted by static friction faults. Emphasizing the significance of fault tolerance in spacecraft hardware, we ascertain the threshold at which component functionality is substantially compromised. Using the Rolling Root-Mean-Square (RRMS) of the reaction wheel's static friction profile over time as Feature Data (FD) within a 10-minute time frame for two fault scenarios - one-time and repeated occurrences, our analysis demonstrates a direct relationship between fault instances and FD escalation. This correlation is further elucidated by integrating Fault-to-Failure Progression (FFP) FD into the Adaptive Remaining Useful Life Estimator (ARULE) for prognostic assessment, shedding light on the challenges and ramifications of mechanical faults on attitude control systems. ARULE predicts complete degradation in both fault cases within 500 mins of spacecraft flight time. Our study underscores the pivotal role of predictive analytics in spacecraft health management, particularly in optimizing performance and prolonging the service life of critical hardware amidst operational challenges in orbit.**

I. Introduction

Space missions are complicated and require extreme precision of attitude control [1]. While it is possible to have a scenario where attitude control is required only during certain portions of the trajectory or even phases, nonetheless, attitude control is a critical aspect and task for any spacecraft. Actuators to control the attitude are selected depending on the size of the spacecraft and mission profile. The most commonly used mechanisms for attitude control are the momentum exchange devices. Within this category, the Variable Speed Control Moment Gyroscopes (VSCMGs) are most efficient. However, the increased complexity and failure points make it a secondary choice. Reaction wheels are the most popular and used devices for attitude control on-board spacecrafts. The guidance module typically computes the attitude error based on sensor fusion of gyroscopic measurements with an online estimator such as a Kalman filter, and drives the reaction wheels to achieve zero attitude error. Full three-axis control generally comprises of three or more reaction wheels. Commonly used configurations include a NASA configuration and a pyramid configuration. As with any mechanical system or device, the reaction wheels are also susceptible to failure. These failures do not immediately result in non-operational status of the wheels, but increase wear of the device [2]. Prolonged use of these devices under fault leads to faster degradation and total physical failure. Thus, it becomes crucial to predict the Remaining Useful Life (RUL), Prognostic Horizon (PH), and State-of-Health (SoH) of these devices. Machine learning (ML) algorithms have been used to detect the fault apriori and produce prognostic estimates [3] [4] [5]. However, several challenges must be addressed to leverage ML effectively in space missions.

One of the primary challenges is the quality of data available for training ML models. Space missions often operate with limited datasets due to the high cost and duration constraints. Obtaining sufficient labeled data for training ML models can be challenging, and telemetry data may contain noise or uncertainties due to environmental factors or sensor inaccuracies [6]. Interpretability is another critical challenge in the adoption of ML for spacecraft applications. Many ML algorithms such as deep neural networks are considered black box models making it difficult to interpret their decision-making processes. This lack of transparency can pose challenges in gaining trust and understanding the behavior of ML-based systems, especially in safety-critical applications like spacecraft operations [7]. Additionally, computational resources onboard spacecraft are often limited, including processing power and memory. ML algorithms deployed for real-time processing of telemetry data must be computationally efficient and lightweight to operate within these constraints. Furthermore, ML models must be capable of making timely predictions within the constraints of spacecraft operations, requiring optimization for speed and efficiency [8]. Generalization and adaptation of ML models present further challenges. ML models trained on historical data must generalize well to unseen scenarios and environments encountered during space missions. Moreover, space environments are dynamic, and ML models must adapt to changes in operating conditions, sensor characteristics, and spacecraft dynamics to maintain their performance and reliability over mission duration [9].

Reaction wheels can fail in various ways, including bearing wear, lubrication issues, or electronics failure. Each failure mode (FM) has its unique set of condition indicators (CIs), making it challenging to develop a one-size-fits-all algorithm for real-time on-orbit monitoring. A sophisticated Failure Modes and Effects Analysis (FMEA) is required to build a library of FMs and explore their complexities. In many spacecraft designs, reaction wheels are critical components, and redundancy may be limited due to constraints such as mass, volume, and power. In case of failure, the spacecraft may have limited backup systems, making it crucial to accurately predict RUL to plan for potential replacements or adjustments in operations. Reaction wheel performance can change over time due to wear, making it challenging to rely solely on static models. Incorporating adaptive modeling techniques that can adjust to changing conditions and performance degradation is crucial for accurate real-time assessments.

In this paper, we present a proof-of-concept for predicting the prognostic estimates of reaction wheels undergoing two different fault scenarios - one-time fault and repeated faults using Ridgetop's Adaptive Remaining Useful Life Estimator [10], a predictive analytics software tool compliant with IEEE 1856-2017 PHM Standard Framework for Prognostics and Health Management of Electronic Systems [11]. Given sensor feature data that are above a predefined "good-as-new" floor and below a "failed" ceiling, ARULE employs an advanced prediction method related to Extended Kalman filtering (EKF) to produce new RUL, SoH, and PH estimates for each sensor data point. The software is run using an intuitive graphical user interface (GUI) or a command-line interface (CLI) that allows a user to upload and process condition-based data (CBD) streams for a target system or subsystem whose health is to be monitored. The software platform relies on user-specified system definition and node files, and key parameters to process the condition-based data. Once the data inputs and parameters are entered into the program, it outputs key prognostic estimates and data plots for RUL, SoH, and PH.

Here, we present operational principles of reaction wheels to derive the motor torque equation that relates to the rise in temperature due to static friction. Subsequently, we briefly introduce ARULE that takes Fault-to-Failure Progression (FFP) or Condition Indicator (CI) Feature Data (FD) as input and estimates the aforementioned key prognostic estimates. Finally, a low Earth orbit (LEO) scenario is considered for generating synthetic data using Basilisk, an open-source astrodynamics simulation framework. The faults are injected and the synthetic data consisting of two fault occurrence cases, one-time and repeated, are fed into ARULE for further analysis.

II. Problem Statement and Foundation

Faults are dangerous for space missions and depending on the severity, time, and frequency of occurrence, these faults may lead to a total mission failure. Reaction wheels are robust momentum exchange devices that transfer momentum of the spacecraft by exerting a torque on the rigid body. However, they may experience faults during their lifetime due to extended operation times beyond set mission timelines, excessive radiation, or mechanical failures. These faults can be classified either as mechanical or electrical. Any failure in the bearing increases friction, leading to increasing temperature, and damage to wheels and nearby components. Imbalanced reaction wheels increase vibrations and affect the spacecraft's stability and positional accuracy. Electrical faults often manifest as over-current conditions in reaction wheel's motor. Issues in the power supply, control electronics, or the motor itself can lead to such faults. Extended over-current draw results in increased heat generation catalyzing mechanical wear and reducing efficiency. Circuit failures can lead to incorrect speed commands or feedback, disrupting control algorithms, and leading to erratic wheel behavior. In any fault condition, temperature is bound to rise. As such, increasing temperature is a common symptom of wear, and ought to be monitored.

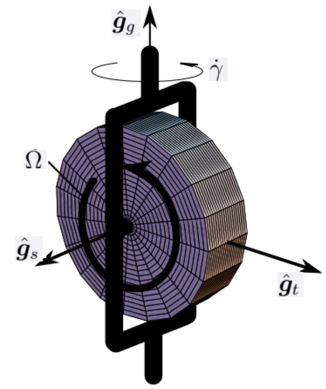

Fig. 1. Coordinate frame, gimbal frame, $\mathcal{G}:\{\hat{\boldsymbol{g}}_s,\hat{\boldsymbol{g}}_t,\hat{\boldsymbol{g}}_g\}$ for a VSCMG [12]. The wheel speed is denoted by Ω and gimbal rate by $\dot{\gamma}$.

A. Principle of Reaction Wheel Operation

Consider three coordinate frames: reaction wheel frame, body frame, and inertial frame. The reaction wheel frame is defined as $\mathcal{W}:\{\hat{\boldsymbol{w}}_s,\hat{\boldsymbol{w}}_t,\hat{\boldsymbol{w}}_g\}$ where $\hat{\boldsymbol{w}}_s$ points in the direction about which the reaction wheel spins, $\hat{\boldsymbol{w}}_t$ is along the radial direction, and $\hat{\boldsymbol{w}}_g$ completes the orthogonal vector set. The body frame is defined as $\mathcal{B}:\{\hat{\boldsymbol{b}}_1,\hat{\boldsymbol{b}}_2,\hat{\boldsymbol{b}}_3\}$ where each axis of the frame aligns with the principal body axes. The final frame, inertial frame, is defined as $\mathcal{N}:\{\hat{\boldsymbol{n}}_1,\hat{\boldsymbol{n}}_2,\hat{\boldsymbol{n}}_3\}$. Note that the reaction wheel operation is a special case of VSCMG in absence of gimbaling. If γ denotes the angle by which the VSCMG has turned about the hinged axis, then the gimbaling rate is denoted by $\dot{\gamma}$. For no gimbaling rate, $\dot{\gamma}=0$, a VSCMG operates as a reaction wheel. Figure 1 shows a VSCMG with the gimbal frame $\mathcal{G}:\{\hat{\boldsymbol{g}}_s,\hat{\boldsymbol{g}}_t,\hat{\boldsymbol{g}}_g\}$. The gimbal and reaction wheel frame share the spin axis, $\hat{\boldsymbol{w}}_s=\hat{\boldsymbol{g}}_s$. Therefore, an alternative form of reaction wheel frame is $\mathcal{W} : \{\hat{\boldsymbol{g}}_s, \hat{\boldsymbol{w}}_t, \hat{\boldsymbol{w}}_g\}$.

Denoting the inertia of the reaction wheel disk as $[I_W]$ (inertia matrix) and that of the spacecraft's rigid body as $[I_s]$, the total inertia of the spacecraft is then given by $[I] = [I_s] + [I_W]$. The angular momentum of the reaction wheel and spacecraft is given by:

$$\boldsymbol{H}_W = [I_W]\boldsymbol{\omega}_{\mathcal{W}/\mathcal{B}} \tag{1}$$

$$\boldsymbol{H}_B = [I_s]\boldsymbol{\omega}_{\mathcal{B}/\mathcal{N}} \tag{2}$$

where $\boldsymbol{\omega}_{\mathcal{W}/\mathcal{B}}$ is the reaction wheel speed with respect to the spacecraft body frame and $\boldsymbol{\omega}_{\mathcal{B}/\mathcal{N}}$ is the rotational rate of the spacecraft with respect to the inertial frame. Defining $\boldsymbol{\omega}_{\mathcal{W}/\mathcal{N}} = \boldsymbol{\omega}_{\mathcal{W}/\mathcal{B}} + \boldsymbol{\omega}_{\mathcal{B}/\mathcal{N}}$, the total angular momentum of the spacecraft is [12]:

$$\begin{aligned} \boldsymbol{H} &= \boldsymbol{H}_B + \boldsymbol{H}_W \\ &= [I_s]\boldsymbol{\omega}_{\mathcal{B}/\mathcal{N}} + [I_W]\boldsymbol{\omega}_{\mathcal{W}/\mathcal{N}} \end{aligned} \tag{3}$$

Under the assumptions of – (a) time-invariant spacecraft inertia, $[\dot{I}] = 0$, and (b) absence of any external force acting on the system $\boldsymbol{F}_{ext} = \boldsymbol{\tau}_{ext} = \boldsymbol{0}$, the torque on the spacecraft is generated only when $\boldsymbol{\omega}_{\mathcal{W}/\mathcal{N}} \neq \boldsymbol{0}$. The change in reaction wheel speed changes its angular momentum, $\dot{\boldsymbol{H}}_W \neq \boldsymbol{0}$. Since the total angular momentum is conserved, $\dot{\boldsymbol{H}} = \boldsymbol{0}$, the angular momentum of the spacecraft must change. If the spin rate of the wheel is Ω and $\hat{\boldsymbol{g}}_s$ is the spin axis, then $\boldsymbol{\omega}_{\mathcal{W}/\mathcal{B}} = \Omega\hat{\boldsymbol{g}}_s$. The equation of motion for the reaction wheel is computed using Euler's equation $\dot{\boldsymbol{H}}_W = \boldsymbol{L}_W$. Using transport theorem to find $\dot{\boldsymbol{H}}_W$:

$$\begin{aligned} \dot{\boldsymbol{H}}_W &= [I_W]\dot{\boldsymbol{\omega}}_{\mathcal{W}/\mathcal{N}} + \boldsymbol{\omega}_{\mathcal{W}/\mathcal{N}} \times \boldsymbol{\omega}_{\mathcal{W}/\mathcal{N}} \\ &= [I_W](\dot{\boldsymbol{\omega}}_{\mathcal{W}/\mathcal{B}} + \dot{\boldsymbol{\omega}}_{\mathcal{B}/\mathcal{N}}) \end{aligned} \tag{4}$$

As the reaction wheel spins about one axis only, it is convenient to assign reaction wheel frame to the inertia tensor. The disk inertia is then expressed as:

$$^{\mathcal{W}}[I_W] = \begin{bmatrix} I_{W_s} & 0 & 0 \\ 0 & I_{W_t} & 0 \\ 0 & 0 & I_{W_t} \end{bmatrix} \tag{5}$$

The inertia about second and third axis is same due to symmetry for a balanced wheel. Expressing the transformation/rotation matrix between the body and wheel frame as $[BW] = [\hat{\boldsymbol{g}}_s \;\; \hat{\boldsymbol{w}}_t \;\; \hat{\boldsymbol{w}}_g]$:

$$\begin{aligned} ^{\mathcal{B}}[I_W] &= [BW]^{\mathcal{W}}[I_W][BW]^T \\ &= I_{W_s}\hat{\boldsymbol{g}}_s\hat{\boldsymbol{g}}_s^T + I_{W_t}\hat{\boldsymbol{w}}_t\hat{\boldsymbol{w}}_t^T + I_{W_t}\hat{\boldsymbol{w}}_g\hat{\boldsymbol{w}}_g^T \end{aligned} \tag{6}$$

Decomposing the inertial rotational body rate in the wheel frame and equating $\boldsymbol{\omega}_{\mathcal{B}/\mathcal{N}} = \boldsymbol{\omega}$:

$$^{\mathcal{W}}\boldsymbol{\omega} = \omega_s\hat{\boldsymbol{g}}_s + \omega_t\hat{\boldsymbol{w}}_t + \omega_g\hat{\boldsymbol{w}}_g \tag{7}$$

Substituting inertia and angular rate expressions in Euler equation for reaction wheel:

$$\begin{aligned} \dot{\boldsymbol{H}}_W &= (I_{W_s}\hat{\boldsymbol{g}}_s\hat{\boldsymbol{g}}_s^T + I_{W_t}\hat{\boldsymbol{w}}_t\hat{\boldsymbol{w}}_t^T + I_{W_t}\hat{\boldsymbol{w}}_g\hat{\boldsymbol{w}}_g^T)(\dot{\Omega}\hat{\boldsymbol{g}}_s + \dot{\boldsymbol{\omega}}) \\ &= I_{W_s}\hat{\boldsymbol{g}}_s\hat{\boldsymbol{g}}_s^T(\dot{\Omega}\hat{\boldsymbol{g}}_s + \dot{\boldsymbol{\omega}}) + I_{W_t}(\hat{\boldsymbol{w}}_t\hat{\boldsymbol{w}}_t^T + \hat{\boldsymbol{w}}_g\hat{\boldsymbol{w}}_g^T)\dot{\boldsymbol{\omega}} \\ &= I_{W_s}(\dot{\Omega} + \hat{\boldsymbol{g}}_s^T\dot{\boldsymbol{\omega}})\hat{\boldsymbol{g}}_s + (I_{W_t}\hat{\boldsymbol{w}}_t^T\dot{\boldsymbol{\omega}})\hat{\boldsymbol{w}}_t + (I_{W_t}\hat{\boldsymbol{w}}_g^T\dot{\boldsymbol{\omega}})\hat{\boldsymbol{w}}_g \end{aligned} \tag{8}$$

The torque about the spin axis is the reaction wheel (RW) motor torque required to spin the wheel. Using short-hand notation, we can express above equation as:

$$\dot{\boldsymbol{H}}_W = \boldsymbol{L}_W = u_s\hat{\boldsymbol{g}}_s + u_t\hat{\boldsymbol{w}}_t + u_g\hat{\boldsymbol{w}}_g \tag{9}$$

$$u_s = I_{W_s}(\dot{\Omega} + \hat{\boldsymbol{g}}_s^T\dot{\omega}) \tag{10}$$

Given the current disk angular acceleration and spacecraft angular acceleration, u_s is the RW motor torque. Note that this expression does not include any effects of gimbaling and thus reflects pure reaction wheel operation.

B. Power and Temperature Consideration

Let the total electrical power drawn by a reaction wheel be P_{elec}. This electrical power is converted to mechanical power and during this process, losses occur due to friction and the electrical resistance of the copper winding. Denoting copper winding losses as P_{Cu}, frictional losses as P_{f}, and mechanical power as P_{mech}:

$$P_{\text{elec}} = P_{\text{mech}} + P_{\text{f}} + P_{\text{Cu}} \tag{11}$$

An equation for electrical power draw for a DC, steady state motor is given in literature [13][14]. The actual mechanical power used to drive the wheel is based on motor efficiency. Considering the electrical power as the input (P_{input}) and mechanical power as output (P_{output}), the motor efficiency can be defined as, η:

$$\eta = \frac{P_{\text{output}}}{P_{\text{input}}} \times 100 \tag{12}$$

Using motor efficiency, we can write:

$$P_{\text{mech}} = \eta P_{\text{elec}} \tag{13}$$

$$P_{\text{f}} + P_{\text{Cu}} = P_{\text{mech}}\frac{1-\eta}{\eta} \tag{14}$$

The mechanical power of the reaction wheel depends on the motor torque and the speed at which the wheel is operating [5]:

$$P_{\text{mech}} = \Omega \cdot u_s = \Omega I_{W_s}(\dot{\Omega} + \hat{\boldsymbol{g}}_s^T\dot{\omega}) \tag{15}$$

Additionally, the frictional dissipation of power, which is a result of the mechanical faults, can be expressed as [5]:

$$P_{\mathrm{f}} = \Omega \cdot \tau_f \tag{16}$$

In this study, we only consider the thermal effects of fault, primarily caused by either bearing failure or over-current draw. The energy dissipation due to friction and copper winding loss causes temperature rise. This is the total thermal power, $P_{\text{therm}} = P_{\text{Cu}} + P_{\text{f}}$. A simple Euler integration converts this thermal power to heat [5]:

$$Q = P_{\text{therm}} \Delta t \tag{17}$$

The temperature is directly proportional to the heat in the system. With calibration, the temperature can be associated with the heat generated as:

$$T_{k+1} = T_k + Q\Delta t \tag{18}$$

where we have assumed no energy dissipation. This particular assumption is relevant for small re-entry vehicles that are unmanned and do not have an active thermal management system.

C. Kalman Filter and Extended Kalman Filter

A common method for estimation is to use some form of Kalman filter. Optimal finite-dimensional algorithms for recursive Bayesian estimation can be formulated in a linear-Gaussian case where the functional recursion of following equation becomes the Kalman filter [15]:

$$p(\boldsymbol{x}_k|\boldsymbol{Z}_{k-1}) = \int p(\boldsymbol{x}_k|\boldsymbol{x}_{k-1})\; p(\boldsymbol{x}_{k-1}|\boldsymbol{Z}_{k-1})\; d\boldsymbol{x}_{k-1} \tag{19}$$

$$p(\boldsymbol{x}_k|\boldsymbol{Z}_k) = \frac{p(\boldsymbol{z}_k|\boldsymbol{x}_k)\; p(\boldsymbol{x}_k|\boldsymbol{Z}_{k-1})}{p(\boldsymbol{z}_{\boldsymbol{k}}|\boldsymbol{Z}_{k-1})} \tag{20}$$

where $p(\boldsymbol{x}_k|\boldsymbol{Z}_{k-1})$ is the prediction density, $p(\boldsymbol{x}_k|\boldsymbol{x}_{k-1})$ is transitional density, $p(\boldsymbol{x}_k|\boldsymbol{Z}_k)$ is posterior probability density function, $p(\boldsymbol{z}_k|\boldsymbol{x}_k)$ is likelihood function, $\boldsymbol{z}_k$ are measurements, $\boldsymbol{Z}_k$ is the sequence of all available measurements. The Kalman filter assumes that posterior density at every time step is Gaussian, hence exactly and completely characterized by its mean and covariance [15]. However, the Kalman filter only applies to linear systems, while many systems encountered in reality exhibit nonlinear behavior. Nonlinear systems are handled using an extended Kalman filter (EKF), which linearizes the system's behavior about a Kalman filter estimate based on a linearized system [16]. Originally proposed by Stanley Schmidt, the extended Kalman filter (EKF) was developed so the Kalman filter could be applied to nonlinear spacecraft navigation problems [16].

D. ARULE Framework

ARULE is a part of Ridgetop's three-stage PHM system architecture shown in Figure 2, which can be used to conceptualize different types of FD extracted from different CBD, stored in files, and subsequently used for post–processing to determine the health, service, and maintenance needs for a given system. It is comprised of the following three stages which are compliant with operational processes and functional blocks of IEEE 1856-2017 [11]:

1) Sensing Stage - Monitor a system node or a collection of nodes that sense and collect CBD indicative of damage or degradation. Corresponds to S and DA in Figure 3.
2) Feature Extraction Stage - Application-specific data processing routines that condition and transform CBD into Feature Data (FD) in a form or signature that is correlated to increasing levels of damage leading to functional failure. Corresponds to DA and DM in Figure 3.
3) Prognosing Stage - Process input Functional Failure Signature (FFS) data to prognose a future time of functional failure and outputs prognostic information such as RUL, PH, and SoH. Corresponds to SD, HA, and PA in Figure 3.

Aside from these three stages, the two right-most blocks following the final stage in Figure 2 correspond to AG and HA in Figure 3.

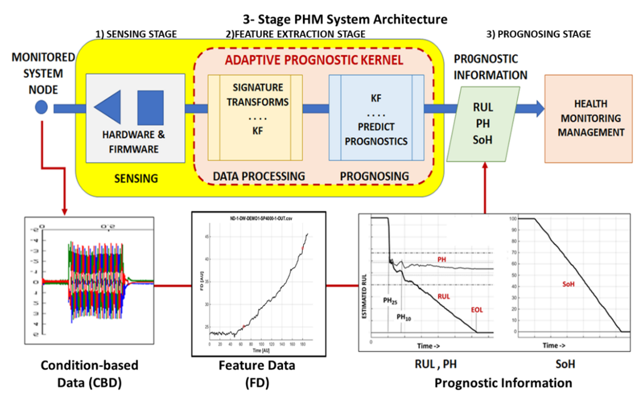

Fig. 2. Diagram of a 3-stage PHM system: (1) sensing stage, (2) feature extraction stage, and (3) prognosing stage to produce prognostic information with ARULE.

The sensing stage is one or more system nodes being monitored for health and is comprised of one or more sensors that monitor nodes by collecting condition-based data (CBD). These sensors can be electrical, mechanical, frequency-based, and so on. As an example from this study, a monitored system node is the reaction wheel location that experiences minimal shock and vibration. CBD examples could include vibration, shock, temperature (heat), light, and electrical (voltage and current). Noisy data, sampling rates, sampling periods, and so on can impact this sensing stage. Therefore, it is important that the output of this stage usually be filtered or windowed.

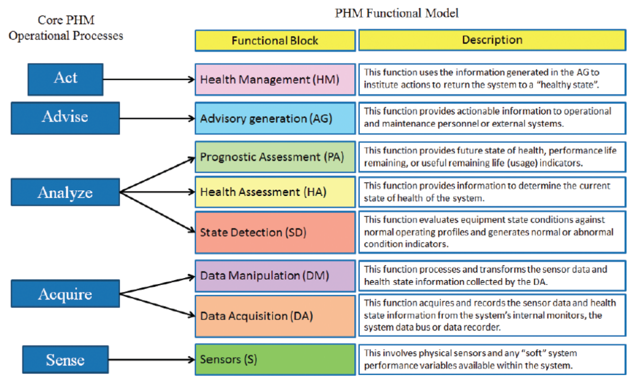

Fig. 3. IEEE 1856-2017 PHM Standard Framework.

Subsequently, the Feature Extraction Stage accepts one or more CBD inputs from sensors attached to system nodes. This stage performs application-specific data processing to extract various types of features (FD) that correlate with system degradation caused by one or more failure modes. Extraction of features from CBD to form signatures is accomplished using any application-specific data-processing algorithms and techniques including classical model-based and data-driven approaches such as reliability analysis, distribution analysis, physics-of-failure modeling, statistical analysis, and machine learning. Examples include:

1) k-nearest-neighbor (KNN) comparisons to identify and select features of interest,
2) distance calculations such as Euclidean or Mahalanobis to determine magnitude of changes in measurements related to damage/degradation,
3) and physics-of-failure models to determine changes in parameter values correlated with increasing damage/degradation.

The objective of this stage is to extract features (FD) that form a signature comprising changes in value correlated with increasing levels of damage/degradation. In the absence of degradation, FD data forms an essentially flat signature, whereas in the presence of degradation, FD data forms a curvilinear signature.

At the core of this three-stage architecture is the ARULE Adaptive Prediction Kernel (APK), which is comprised of two subsystems: Data Processing and Prognosing. The Data Processing subsystem transforms FD signatures into other signatures upon request from a feature extraction stage. The signature transformation occurs sequentially, one data point at a time, rather than through batch-mode processing of an entire dataset, allowing for near real-time prognostic results. To accommodate robust extraction and/or data processing, the feature extraction stage can specify the step at which signature processing begins and the parameter values to be used in signature processing. The steps taken by this subsystem are as follows:

1) Transform FD signature data into Fault-to-Failure Progression (FFP) signature data.
2) Transform FFP signature data into Degradation Progression Signature (DPS) data.
3) Transform DPS data into Functional Failure Signature (FFS) data.

Secondary functions of this subsystem include performing noise mitigation, such as data smoothing and noise margin adjustments, upon request.

Next, the Prognostics subsystem accepts and processes FFS data to produce prognostic information: Remaining Useful Life (RUL), State of Health (SOH), and Prognostic Horizon (PH). The Prognostics subsystem comprises algorithms designed to rapidly and accurately converge to the prediction of the true time of functional failure, identifying the point in time where a prognostic target is no longer capable of operating within specifications.

III. Analysis of Low Earth Orbit Scenario

Consider a spacecraft or satellite in Low Earth Orbit (LEO). The actuators for attitude control are four reaction wheels in pyramid configuration. The initial conditions for the spacecraft are listed in Table I. The attitude is described using Modified Rodrigues Parameters (MRPs). The Modified Rodrigues Parameters (MRPs) are attitude parameters represented by vector $\boldsymbol{\sigma} = [\sigma_1 \quad \sigma_2 \quad \sigma_3]^T$. In this scenario, the spacecraft is assigned to operate in hill pointing mode for 500 mins. The reaction wheels used are Honeywell HR16 model with 50 Nms maximum angular momentum storage. The simulation is performed using Basilisk, an open-source astrodynamics simulation framework [17]. Basilisk has an in-built thermal and encoder module [5]. Under nominal operation, the reaction wheels must have zero static friction, drive attitude error to zero within numerical precision, and not have erratic speed transition. Under no faults and with assumption of accurate reaction wheel sizing, the reaction wheel cluster must be able to control the attitude of the spacecraft.

A. Fault Simulation

A friction fault would increase the nominal static friction of the reaction wheel by a factor between five and twenty [5]. This friction increase must be overcome by the motor to achieve the commanded reaction wheel speed. Two scenarios are baselined in this paper for assessment. In the first scenario, we artificially inject only one fault during the whole duration on one reaction wheel. In the second scenario, we inject multiple faults to the same reaction wheel. Fault injection time is randomized using uniform distribution. The simulation is setup in Basilisk where the static friction fault is injected. For illustrative purpose, the static friction increase for one time fault is increased by a factor of five, whereas for repeated faults, the increase is more gradual and randomized to show the cumulative effect on the wheel's

TABLE I
INITIAL CONDITIONS FOR BASILISK SIMULATION

Parameter	Value	Unit
a	10000.0	km
e	0.1	-
i	33.3	deg
Ω	48.2	deg
ω	347.8	deg
f	85.3	deg
$\sigma_{\mathcal{B}/\mathcal{N}}$	[0.1, 0.2, -0.3]	-
${}^{B}\boldsymbol{\omega}_{BN}$	[0.01, -0.01, 0.03]	rad/s

operation. In our analysis of the Low-Earth Orbit scenario, we exclude stochastic variability from the addition of Gaussian noise to input parameters that may obscure the deterministic relationships we aim to investigate.

B. One-Time and Repeated Faults

Figure 4 illustrates the reaction wheel speed of a selected component from the cluster under different operational scenarios. Under normal conditions, the speed exhibits a pure sinusoidal pattern. However, in the presence of faults, such as one-time and repeated occurrences, the speed drops abruptly to zero. This decline in speed initiates immediately upon fault detection, attributed to angular deceleration governed by the static friction value.

In Figure 5, we compare the static friction for one-time and repeated faults, observing a cumulative effect with repeated occurrences. Once a fault is detected, wheel operation is impeded, causing the speed to fall. Although this doesn't instantaneously halt the reaction wheel, a noticeable transient effect is evident. Upon complete cessation of wheel movement, it becomes non-operational, necessitating the remaining three reaction wheels to compensate for attitude error convergence.

Attitude error, denoted by $\boldsymbol{\sigma}_{\mathcal{B}/\mathcal{R}}$, represents the disparity between the desired orientation of a spacecraft (body frame $\mathcal{B}$) and its actual orientation (reference frame $\mathcal{R}$). Successful attitude control requires driving this error to zero:

$$\boldsymbol{\sigma}_{\mathcal{B}/\mathcal{R}} = \boldsymbol{\sigma}_{\mathcal{B}} - \boldsymbol{\sigma}_{\mathcal{R}} \rightarrow 0 \tag{21}$$

Under fault-free conditions, the attitude error norm steadily converges to zero. However, in fault scenarios, we observe a significant deviation in attitude convergence, as depicted in Figure 6. Faults restrict the actuators' ability to converge attitude error efficiently.

Despite the hindered convergence, additional fault occurrences on the same wheel do not affect the operation of the remaining active wheels significantly. Consequently, attitude convergence may take longer, albeit not substantially. The

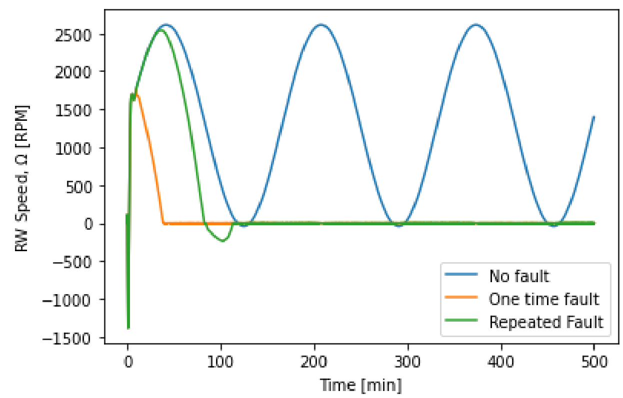

Fig. 4. Reaction wheel speed variation over time during hill pointing mode.

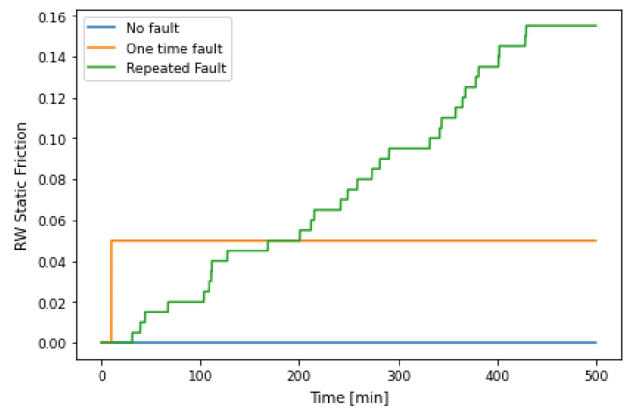

Fig. 5. Static friction variation over time for one time and repeated fault compared to nominal value.

initial convergence delay is attributed to a marginal increase in friction value, which initially does not impede attitude error convergence. However, once the friction exceeds a certain threshold, about a factor of two and a half times pristine friction, the wheel's speed diminishes rapidly, leading to a transient increase in attitude error.

This synthetic simulation data serves as a foundation for post-processing. It represents Condition-based Data (CBD) from which features are extracted and input into ARULE for analysis. ARULE then renders predictions on Remaining Useful Life (RUL), Prognostic Horizon (PH), and State of Health (SoH), aiding in proactive maintenance strategies.

C. ARULE Inputs & Outputs

To comprehensively characterize the Fault-to-Failure Progression (FFP), we employed the Rolling Root-Mean-Square (RRMS) technique, as depicted in Equation 22, where k is the time window size in minutes, and $x_1^2, x_2^2, x_3^2, ..., x_n^2$ denote the squared signal values. For this analysis, we utilized a time window of 10 minutes.

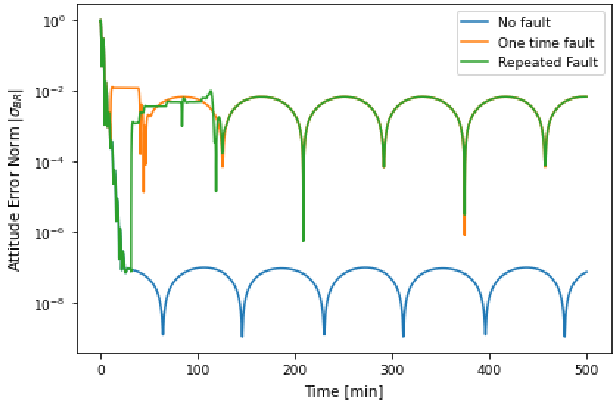

Fig. 6. Variation of attitude error over time. For nominal operation, the attitude error is driven to zero with higher numerical precision.

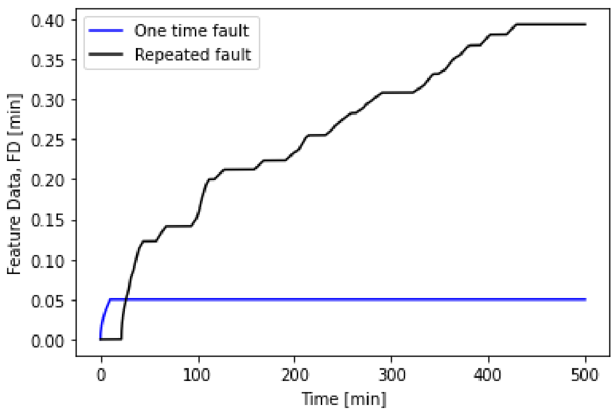

Fig. 7. Rolling Root-Mean-Square (RMS) Feature Data (FD) calculated for one time and repeated fault scenarios.

This approach facilitated the extraction of Feature Data (FD) for both instances of failure occurrences, as shown in Figure 7. While the FD curve for the one-time fault scenario may not have precisely aligned with the ideal FFP curve, the curve for repeated faults exhibits a continuous curvilinear signature. This observation underscores a direct correlation between the frequency of faults and the escalation of FD values.

$$\mathrm{RRMS}_i = \sqrt{\frac{1}{k}\left(x_i^2 + x_{i-1}^2 + \ldots + x_{i-k+1}^2\right)} \tag{22}$$

Subsequently, the analysis extends to the integration of this RRMS FD into a Node Definition File (NDEF) inside a System Definition File (SDEF). Within ARULE, SDEF is a high-level overview of the entire system, whereas NDEF is a structured data format used to define the nodes within the system and their parameters, facilitating the organization and processing of FD for prognostic estimation. In the prognostic degradation model, the baseline FD value, indicative of a system devoid of any degradation, was established at 0.001. In the one-time and repeated-fault cases, the FF threshold was determined to

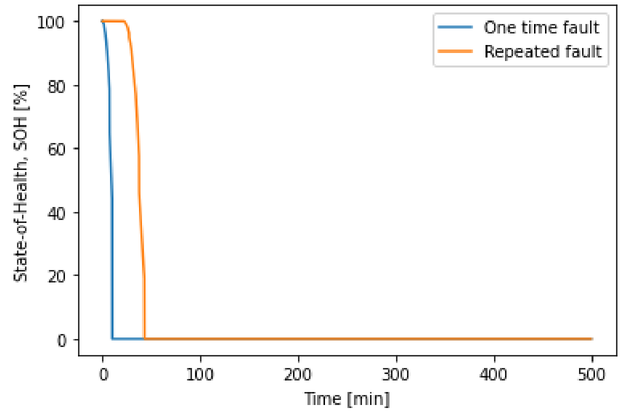

Fig. 8. State of Health (SoH) of reaction wheels for one time and repeated fault scenarios.

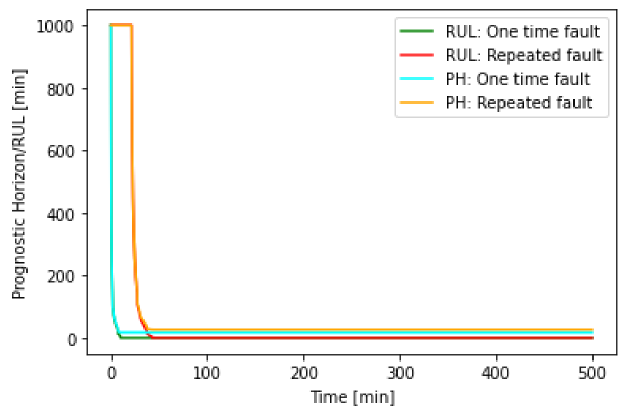

Fig. 9. Remaining Useful Life (RUL) and Prognostic Horizon (PH) of reaction wheels for one time and repeated fault scenarios.

be a 1100% increase in FD, setting a critical value of 0.11. FF represents the point at which the system can no longer operate nominally. The Time-To-Functional Failure (TTFF) was initially estimated at 1000 minutes, providing a forecast for the duration until the system reaches its FF threshold under current conditions. Given the synthetic nature of the dataset, devoid of the noise typically present in real-world data, the noise margin was set to zero. This decision reflects the controlled conditions under which the FD were generated and analyzed, thereby ensuring the precision of prognostic estimations. Shown in Figure 8 and Figure 9 are the SoH and the RUL/PH for both cases, respectively. Results shown suggest that the system undergoes complete failure at 9.808 minutes for the one-time fault scenario and 42.78 minutes for the repeated faults scenario. These cases can be treated as two FMs for spacecraft reaction wheels.

IV. Conclusion

This paper emphasizes the significance of prognostic evaluations of FFP signatures in spacecraft reaction wheel systems. Simulated synthetic reaction wheel static friction data from a spacecraft in LEO was used as CBD, and a RRMS analysis over a 10 minute window was carried out to extract FD. The continuous increase in FD with repeated faults demonstrates a direct correlation with fault frequency, highlighting the importance of monitoring and managing these parameters to mitigate failure risks. These FD were input into ARULE to enable further processing for prognostic estimates, revealing the intricate relationship between static friction, operational degradation, and system failure thresholds using RUL, PH, and SoH. In both cases of fault occurrences - one-time and repeated, a complete reaction wheel failure is predicted within the first 50 minutes of the spacecraft's flight time.

A single instance of increased static friction can significantly impact the reaction wheel's performance, emphasizing the necessity of real-time monitoring and predictive maintenance for extending operational life. The use of ARULE to process FD from fault simulations provides valuable insights into the prognostic health management of spacecraft reaction wheels. This approach enhances understanding of FFP signatures and offers a robust methodology for predicting system degradation and optimizing maintenance schedules. Using this methodology, multiple reaction wheels can be monitored in real time, and useful FD and CIs obtained in their raw data streams can be passed to ARULE for determination of RUL, PH, and SoH, as the spacecraft carries its mission on-orbit. Integrating advanced data analysis techniques with predictive health management tools is crucial for ensuring the reliability and longevity of critical spacecraft components. These methodologies and insights will be instrumental in safeguarding mission success amid inevitable component faults during ongoing space exploration.

References

[1] F. L. Markley and J. L. Crassidis, *Fundamentals of spacecraft attitude determination and control*. Springer, 2014, vol. 1286.

[2] L. Xiao and J. Zhang, "Review of fault diagnosis and fault-tolerant control technologies for aerospace systems," *Progress in Aerospace Sciences*, vol. 80, pp. 1–14, 2016.

[3] L. A. Gagg Filho *et al.*, "Artificial intelligence in fault detection and diagnosis for spacecraft systems: A review," *IEEE Transactions on Aerospace and Electronic Systems*, 2019.

[4] M. S. Islam and A. Rahimi, "A three-stage data-driven approach for determining reaction wheels' remaining useful life using long short-term memory," *Electronics*, vol. 10, no. 19, 2021. [Online]. Available: https://www.mdpi.com/2079-9292/10/19/2432

[5] J. Vaz Carneiro, H. Schaub, M. Lahijanian, K. Lang, and K. Borozdin, "Machine learning for reaction wheel fault detection using simulated telemetry data," in *AIAA SCITECH 2022 Forum*, 2022, p. 2507.

[6] M. K. Mallick and R. B. Amarasingh, "Machine learning techniques for reliability analysis in aerospace systems," *Reliability Engineering & System Safety*, vol. 181, pp. 47–60, 2018.

[7] R. Yan, G. Wang, and F. Jia, "Machine learning approaches for predicting remaining useful life: A review," *Engineering Applications of Artificial Intelligence*, vol. 87, pp. 218–238, 2019.

[8] M. Shahzad, F. Subhan, and S. Hassan, "Prognostics of spacecraft reaction wheels using machine learning," in *2018 International Conference on Computing, Mathematics and Engineering Technologies (iCoMET)*. IEEE, 2018, pp. 1–6.

[9] R. Wang and Y. Wang, "Reliability analysis of spacecraft reaction wheels," in *2015 IEEE Aerospace Conference*. IEEE, 2015, pp. 1–9.

[10] J. P. Hofmeister, K. Goebel, and S. Vohnout, "Adaptive remaining useful life estimator™(arule™)," in *Annual Conference of the Prognostics and Health Management Society*, 2009.

[11] M. Pecht, S. Mathew, L. Gullo *et al.*, "'ieee standard framework for prognostics and health management of electronic systems," *IEEE Standards Assoc., Piscataway, NJ, USA, Tech. Rep*, vol. 2017, p. 2017, 1856.

[12] H. Schaub and J. L. Junkins, *Analytical mechanics of space systems*. Aiaa, 2003.

[13] E. A. Culton and N. P. S. M. C. M. U. States, "Minimum electrical energy spacecraft maneuvers: Theory and experiments," *Naval Postgraduate Scho Monterey United States, Tech. Rep*, 2019.

[14] H. C. Marsh, M. Karpenko, and Q. Gong, "Relationships between maneuver time and energy for reaction wheel attitude control," *Journal of Guidance, Control, and Dynamics*, vol. 41, no. 2, pp. 335–348, 2018.

[15] B. Ristic, S. Arulampalam, and N. Gordon, *Beyond the Kalman filter: Particle filters for tracking applications*. Artech house, 2003.

[16] D. Simon, *Optimal state estimation: Kalman, H infinity, and nonlinear approaches*. John Wiley & Sons, 2006.

[17] P. W. Kenneally, S. Piggott, and H. Schaub, "Basilisk: A flexible, scalable and modular astrodynamics simulation framework," *Journal of aerospace information systems*, vol. 17, no. 9, pp. 496–507, 2020.